THE JOURNAL OF PHYSICAL CHEMISTRY B

Article

Cite This: J. Phys. Chem. B 2018, 122, 11072−11082

pubs.acs.org/JPCB

Disorder at the Tips of a Disease-Relevant Aβ42 Amyloid Fibril: A Molecular Dynamics Study

Ioana M. Ilie* and Amedeo Caflisch*

Department of Biochemistry, University of Zürich, 8057 Zürich, Switzerland

Supporting Information

ABSTRACT: We present a simulation study of the early events of peptide dissociation from a fibril of the Alzheimer's Aβ42 peptide. The fibril consists of layers of two adjacent Aβ42 peptides each folded in an S-shaped structure which has been determined by solid state NMR spectroscopy of a monomorphic disease-relevant species. Multiple molecular dynamics runs (16 at 310 K and 15 at 370 K) were carried out starting from an 18-peptide protofibril for a cumulative sampling of about 15 μs. The simulations show structural stability of the fibrillar core and an overall increase in the twist to about 3 degrees. The N-terminal segment 1−14 is disordered in all peptides. At both ends of the fibril, the central segment 21−29, which includes part of the β_2 strand, dissociates in some of the simulations. The β_1 and β_3 strands, residues 15−20 and 35−41, respectively, are structurally stable. The transient binding of the N-terminal stretch to the β_3 strand of the adjacent peptide at the tip is likely to contribute to the arrest phase of the stop-and-go mechanism.

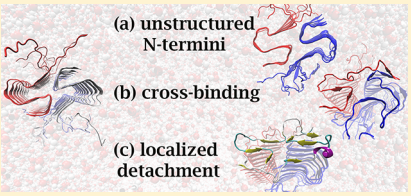

INTRODUCTION

Protein self-assembly is linked to numerous diseases ranging from sickle cell anemia and systemic amyloidosis, for which the toxicity is directly related to mechanical stress, to neurodegenerative disorders, for which the toxic species are still not clear. Sickle cell anemia is a chronic and hereditary disease (with nearly 5 million people affected, mainly in sub-Saharian Africa) which is caused by the polymerization of the mutated form of hemoglobin called hemoglobin S. The self-assembly of folded hemoglobin S molecules into fibrils reduces the flexibility of red blood cells resulting in pain, fatigue, and infections. Among his many seminal contributions to protein biophysics and folding, William A. Eaton has pioneered the development of kinetic models that describe the nucleation and fibrillar growth of deoxyhemoglobin S. His models were able to predict the dependence of the delay time of sickle cell diseases on changes in intracellular hemoglobin S concentration and oxygen saturation.[1,2] Recently, W. A. Eaton proposed five approaches to the inhibition of the polymerization of hemoglobin S,[3] a strategy which would block the root cause of sickle cell diseases rather than the downstream events which are targeted by the currently available drugs. Particularly interesting is the development of small-molecule ligands that should bind tightly to the hemoglobin S surface regions involved in the intermolecular contacts in the fibril.

The neurodegenerative disorders linked to protein aggregation include Parkinson's disease (PD) and Alzheimer's disease (AD), which are characterized by cross-β amyloid fibrils.[4−6] The pathology of AD is characterized, at a neurophysiological level, by the presence of highly insoluble, densely packed, and aggregated peptide filaments, namely extracellular amyloid plaques and intraneuronal fibrillar tangles.[7] The peptides associated with these structures are amyloid-β (Aβ) peptides and τ protein, respectively. The dominant forms of the (Aβ) peptide are 40 and 42 residues long, with the latter being more toxic,[8] aggregating faster,[9] and constituting the dominant species in amyloid plaques.[10]

Recently, two research groups have determined, fully independently, the same structure of a disease-relevant Aβ42 fibril by solid state-NMR spectroscopy.[11,12] The structure consists of two S-shaped protofilaments, each containing of Aβ42 peptides that are in contact at a 2-fold symmetry axis. The fibrillar core of the filaments is formed by six intermolecular β-sheets which originate from three β-strands in each of the two peptides. The β-sheets run in parallel along the fibrillar axis in a cross-β conformation. A similar structure S-shaped topology was recently revealed by cryo-electron microscopy complemented by solid state NMR data which showed that the N-terminus contributes to the cross-β sheet structure.[13] These new, unexplored structures may play a key role in understanding the fine details of amyloid aggregation and aid in the development of successful therapeutic interventions for AD.

While NMR spectroscopy and cryo-electron microscopy are useful to determine static structures, computer simulations can provide details of structural stability and fluctuations. Depending on the nature of the scientific question, coarse grained or atomistic simulations can be carried out. To achieve the long time scales of aggregation, the complexity of a system is reduced by representing peptides as chains of beads or as single particles.[14−21] Coarse-grained models, many of which

Special Issue: William A. Eaton Festschrift

Received: May 31, 2018
Revised: June 29, 2018
Published: July 2, 2018

DOI: 10.1021/acs.jpcb.8b05236
J. Phys. Chem. B 2018, 122, 11072−11082

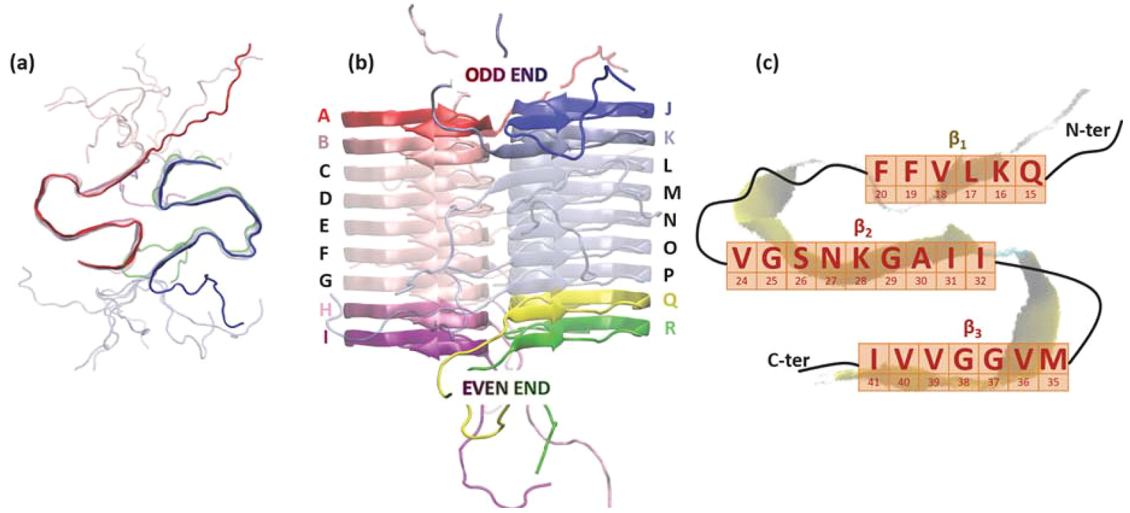

Figure 1. (a) Top- and (b) side-view of the solid-state NMR structure of the monomorphic Aβ42 amyloid fibril (PDB ID: 5KK3[12]). The individual peptides are highlighted by different colors and labeled by capital letters. The color scheme and labels are maintained throughout the article. (c) Top-view cartoon of the red protofilament (PF_1). The annotated residues form the three β-strands.

are purely phenomenological, capture the most relevant properties observed in experiments, and are used to explore aggregation mechanisms and kinetics. Whether disordered or neatly arranged,[14,15,18] amyloid-protected, or amyloid-forming,[16,17] these models frequently distinguish between two or more monomeric states of the peptides by using either geometrical or energetic features. They are used to study the formation pathways of oligomeric and fibrillar structures[16,17] as well as the breakage of filaments.[22] Furthermore, they can reproduce the one-step and two-step nucleation mechanisms of amyloid self-assembly[14,15] and further mechanisms of fibrillar growth.[18]

Coarse grained simulations are unable to explore, in depth, the structural differences between various aggregates and to quantitatively reproduce the structural heterogeneity of amyloid peptides. In contrast, atomistic simulations can provide information on the structural details of both monomeric and aggregated peptides on resolutions that are not achievable by neither experiment or coarse grained models. Implicit solvent simulations have provided evidence that monomeric Aβ adopts a micelle-like architecture in aqueous solution with a weak β-sheet propensity.[23] Explicit solvent simulations have been used to investigate the conformational preferences of intrinsically disordered proteins and peptides in solution[24−26] and inform on the binding/unbinding mechanisms of monomers to fibrillar structures.[24,27] The effect of the mutations on oligomeric and fibrillar stabilities[28] has been also investigated by explicit solvent simulations.[29−31] As an example, a replica exchange molecular dynamics study on the 15−28 fragment of the Aβ peptide showed that the Dutch mutation (E22Q) increases aggregation rates by lowering the barrier for Aβ monomer deposition onto a fibril.[31] Furthermore, the Italian (E22K), Dutch (E22Q), Arctic (E22G), and Iowa (D23N) mutations displayed reduced helix propensity in residues 33−36, while only the Italian and Dutch mutations increased the helix propensity in residues 20−23.[32] Moreover, the effect of osmolytes and denaturants on intrinsically disordered proteins and their role in the regulation of peptide conformation and aggregation have also been widely explored.[33−36]

Here, we use explicit solvent molecular dynamics to study the structural stability and flexibility of the recently published solid-state NMR structure of a disease-relevant Aβ42 amyloid fibril. Multiple 0.5 μs simulations of an 18-meric protofibril show that the structure is preserved, except for a twisting of about 3 degrees along the fibrillar axis. The N-terminal segment is disordered in all of the peptides but can also assume a transient β structure. Furthermore, the peptides at the two fibrillar tips are flexible, while the core peptides are rigid.

MATERIALS AND METHODS

System Preparation. The recent solid state NMR[11,12] and cryo-electron microscopy structures[13] of Aβ42 fibrils are interesting starting points for the simulation studies of Aβ42 self-assemblies. As the starting structure for the present study, we used the model proposed by Colvin et al. (PDB ID: 5KK3).[12] The solid state NMR structure revealed two Aβ42 filaments (highlighted in red and blue in Figure 1a), each shaped as a double horseshoe, with the two horseshoes meeting around a 2-fold axis.[37] Stacks of identical double horseshoes form a single filament, and two filaments are tightly associated along the axis of the fibril (Figure 1b). Residues 15−42 of each monomer form three in register cross-β-strands labeled in the following sections β_1 to β_3. We adopt the notation β_1 for residues Q15−F20, β_2 for V24−I32, and β_3 for M35−I41 throughout this article (Figure 1c). As the side chain orientations are different at the two fibril ends, we call them the odd end (peptides A and J) and the even end (petides I and R), respectively (Figure 1b).

Simulation Protocol. All production simulations were carried out using the GROMACS 2016.3 simulation package[38,39] and the CHARMM36m force field.[40] We first generated 16 independent starting configurations by reconstructing the N-terminal segments for all of the peptides using Monte Carlo sampling. More precisely, the missing N-terminal tails (residues 1−10 in each of the 18 chains) were built initially in an excluded volume-obeying manner using CAMPARIv3 (http://campari.sourceforge.net). This procedure randomizes dihedral angles hierarchically and guarantees that there is no spurious correlation between models at the level of the starting structures. All models were then subjected

DOI: 10.1021/acs.jpcb.8b05236
J. Phys. Chem. B 2018, 122, 11072−11082

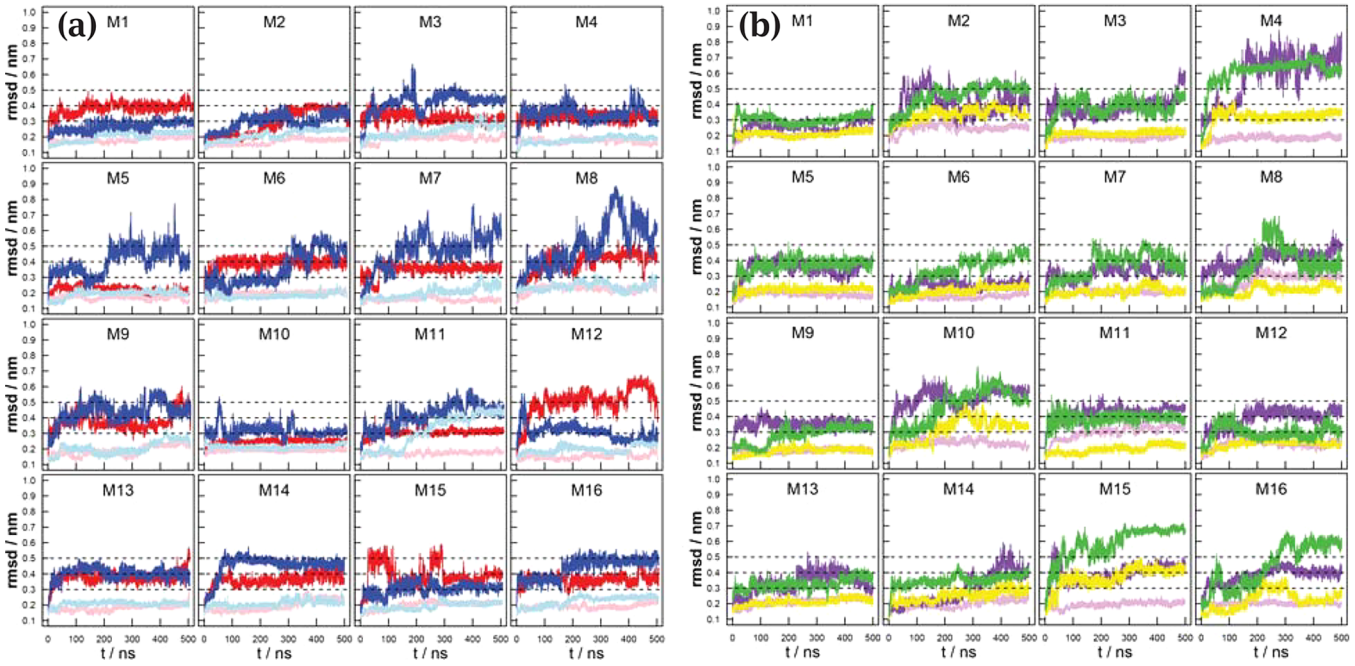

Figure 2. Temporal evolution of the root-mean-square deviation (RMSD) of the tip peptides at (a) the odd end and (b) even end. RMSDs are shown for the surface peptides A, J, I, and R (dark colors) and penultimate peptides B, K, H and Q (pale colors, same color scheme as in Figure 1b). The reference structure is the solid state NMR model (PDB 5KK3[12]). The structural overlap makes use of the C_α atoms of residues 15−42 of the central layers, i.e., peptides C to G and L to P. The RMSD is calculated for the carbon atoms in the backbone and side chains (only those in nonsymmetric groups) as RMSD $= \sqrt{\frac{1}{N}\sum_{i=1}^{N}(\mathbf{r}_i - \mathbf{r}_i^{\mathrm{ref}})^2}$, where $\mathbf{r}_i^{\mathrm{ref}}$ represents the reference position of atom i, and N = 126 carbon atoms belonging to residues 15−42.

to 100000 elementary Monte Carlo steps with a move set consisting of 68.5% pivot moves on side chain dihedral angles, 28.5% pivot moves on backbone ϕ and ψ angles, and 3% pivot moves on ω angles. All but the ω moves used a dual amplitude approach to increase sampling quality.[41] The ω moves were all local with a small step size to avoid *cis*/*trans* isomerization of the peptide bond. This equilibration used the ABSINTH implicit solvent model[42] at a temperature of 300 K with charges taken from the CHARMM36 force field.[43] The equilibration was used to resolve minor remaining problems with the excluded volume randomization. No counterions were included during the construction of the N-terminal segments. During both randomization and equilibration, residues 12−42 in all of the peptides were kept completely frozen. The side chain of E11 was allowed to move during the Monte Carlo equilibration since steric clashes persisted otherwise. Finally, 16 out of the 32 independently generated models were selected upon ranking according to the total energy. To reproduce neutral pH conditions, the N-terminus, lysine, and arginine side chains were positively charged, while the C-terminus, aspartate, and glutamate side chains were negatively charged. All histidine side chains were neutral and protonated at N_δ. Each system was then solvated in a cubic box (edge length of 15.8 nm) with TIP3P water molecules[44] to which 150 mM NaCl were added, including neutralizing counterions (in Gromacs 2016.3). Following the steepest descents minimization, the systems were equilibrated under constant pressure for 5 ns, with position restraints applied on the heavy atoms of the peptides. The temperature and pressure were maintained constant at 310 K and 1 atm, respectively, by using the modified Berendsen thermostat (0.1 ps coupling)[45] and barostat (2 ps coupling).[46] For the production runs, performed in the *NVT* ensemble, all restraints were removed, and the snapshots were saved every 50 ps over a total run length of 500 ns. The short-range interactions were cut off beyond a distance of 1.2 nm, and the potential smoothly decays to zero using the Verlet cutoff scheme. For the electrostatics, the generalized reaction field with an infinite dielectric constant beyond the cutoff of 1.2 nm and a 10 fs update interval for the Verlet buffered neighbor list were used. Bond lengths were constrained using a fourth-order LINCS algorithm with 2 iterations.[47] An integration time step of 2 fs was employed for the simulations at T = 310 K and a time step of 4 fs for the simulations at T = 370 K. The latter was enabled through the use of virtual sites for all hydrogen atoms. The higher temperature is employed to enhance the sampling; the density of water is kept at the value of the 310 K simulations (i.e., same volume of the box and same number of water molecules) to perturb the free energy surface as little as possible.[48,49]

SIMULATION RESULTS

This section focuses on the analysis of the simulations at 310 K. The plots corresponding to the results at 370 K are in the Supporting Information (e.g., RMSD time series in Figures S1 and S2 and twist in Figure S3).

Fibrillar Core Stability and Twist. The 10 peptides in the central section of the protofibrillar structure (peptides C-G and L-P, called core peptides in the following) are structurally stable along all of the simulations at 310 and 370 K with deviations smaller than 0.2 nm (Figure S1). In contrast, variable plasticity is observed at the tips (Figure 2). For both the odd and even ends, the time series of the RMSD show heterogeneous behavior of the surface peptides ranging from negligible deviations from the initial positions (e.g., M10 at the

DOI: 10.1021/acs.jpcb.8b05236
J. Phys. Chem. B 2018, 122, 11072−11082

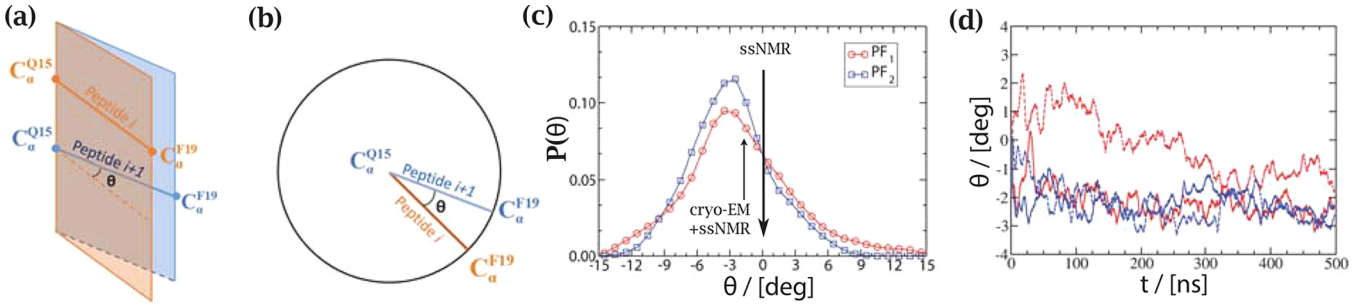

Figure 3. Fibrillar twist. (a) Schematic picture of the twist angle which is the dihedral angle θ defined by the C_α atoms of residues Q15 and F19 of consecutive core peptides i and $i + 1$. (b) Projection along the direction of the protofilament axis to show the twist angle. (c) Distribution of the twist angles for the two protofilaments, PF_1 and PF_2, in red and blue, respectively, averaged over all simulations. The similar distributions indicate convergence of the sampling for the twist. See also Figure S3 for the twist at $T = 370$ K. Vertical arrows indicate the twist as measured in the solid state NMR (ssNMR) structure and cryo-electron microscopy (cryo-EM). (d) Temporal evolution of the twist of two filaments (red and blue) along two runs (solid and dashed lines).

odd end and M1 at the even end) to displacements larger than 0.8 nm (e.g., M8 (Movie M1) and M4 (Movie M2) at the odd and even end, respectively). The peptides in the layer next to the surface peptides (penultimate layer) show minor deviations from the solid state NMR structure, irrespective of the displacement of the tip peptides. This suggests that the peptides in the penultimate layer are much more stable than the surface peptides at the physiological and elevated temperature (Figure S2). In sporadic cases, a large deviation of the surface peptide influences the peptide next to it in the protofilament (e.g., M11 blue and cyan, and M15 green and yellow in Figure 2).

A common feature of amyloid fibrils is the presence of a twist along the direction of the fibrillar axis. In contrast, the solid state NMR structure used as the starting conformation for the simulations does not show any twist, which is probably a consequence of the restraints on the interstrands backbone hydrogen bonds[50] used during structure determination.[11,12] To monitor the twist of the fibril during the simulations, we computed the twist angle between consecutive peptides i and $i + 1$ in each protofilament (Figure 3). For this purpose, we selected the C_α atoms of residues Q15 and F19, and calculated the dihedral angle θ between the planes $\{(C_\alpha^{F19})_i, (C_\alpha^{Q15})_i, (C_\alpha^{Q15})_{i+1}\}$ and $\{(C_\alpha^{Q15})_i, (C_\alpha^{Q15})_{i+1}, (C_\alpha^{F19})_{i+1}\}$. We then averaged over the angles between the core layers, spanning from peptides C to G and L to P. In most simulations and at both temperature values, the negative twist increases within the first 100 ns and reaches a plateau at about −3 degrees (Figure 3d). The probability distribution of the twist has a peak with θ in the range $[-3.5,-2.5°]$ (Figure 3c). Taken together with the interpeptide distance of ≈0.49 nm, the twist values extrapolated along the fibril axis result in a pitch of 50−70 nm, which is comparable to the experimental findings.[51,52]

Fluctuations of the Peptides at the Tips. To analyze deviations from the parallel in-register arrangement we plot the profiles of the average C_α−C_α distance between corresponding residues in the surface peptides and penultimate layer peptides (Figure 4). The profiles along the sequence show a displacement localized at the segment A21-G29 for both tips and at both values of the temperature (see Figure S4 for simulations at 370 K). The segment A21-G29 consists of the loop between strands β_1 and β_2 and most of the latter strand. Its mobility is associated with the partial detachment of the tip peptides from their immediate neighbors (Movies M1−M3). Besides the pronounced flexibility of the segment A21-G29,

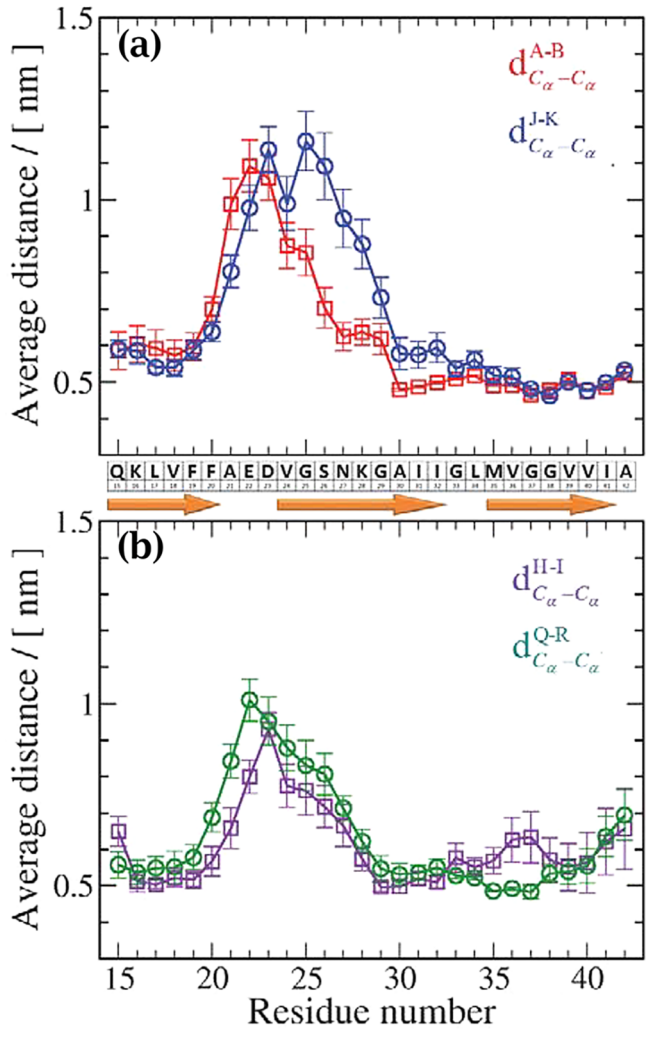

Figure 4. Deviations from the parallel in-register β-sheet structure at the fibril tips. The plot shows the sequence profile of the average C_α−C_α distance between pairs of identical residues in the tip peptide and penultimate layer peptide at (a) the odd end and (b) the even end. The error bars represent the standard error of the mean. The arrows emphasize the three β-strands.

minor displacements are observed for the N-terminal segment of β_1 and the C-terminal segment of β_3. The differences between the two peptides at the same end, e.g., in the position

DOI: 10.1021/acs.jpcb.8b05236
J. Phys. Chem. B 2018, 122, 11072−11082

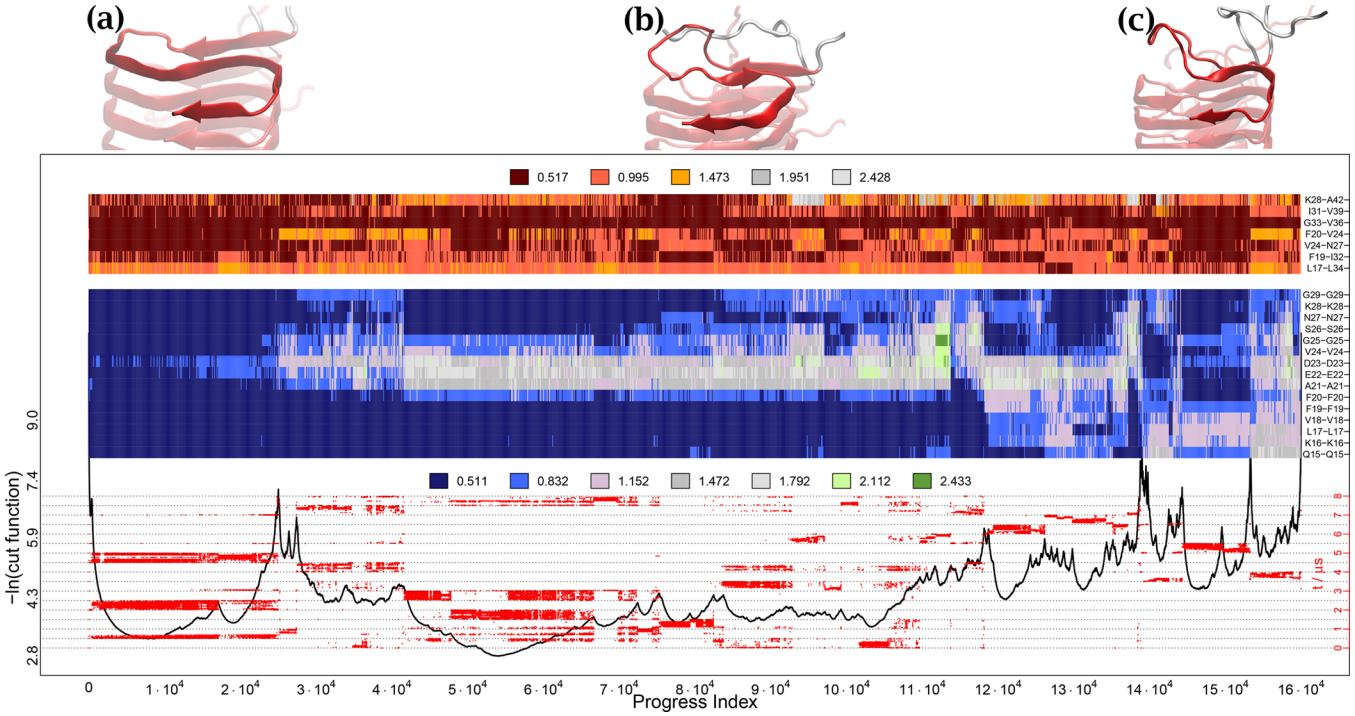

Figure 5. SAPPHIRE plot of the conformational space sampled by peptide A. See the SI for the results at 370 K and peptides J, I, R and AJ IR cumulated (Figures S5 and S8–S12). (Bottom) The progress index corresponds to the reordering of the snapshots according to pairwise structural similarity. The cut function (black line) is constructed by counting transitions along the simulations such that its local minima and maxima correspond to states that are highly populated and barriers that are visited sporadically, respectively. The dynamic trace (red dots with legend on *y*-axis on the right) localizes the time development of the simulated system along the progress index and cut function. In other words, the dynamic trace reflects the sequence of events as it illustrates the visits to individual states and crossing of barriers for each simulation run where individual runs are separated by horizontal dotted lines.(Middle) $C_\alpha-C_\alpha$ distances in nm between peptides A and B. These distances were used for the progress index metric. The structural annotation is binned into seven distances where the shortest (dark blue) corresponds to the optimal interstrand distance and the largest (green) to values larger than 2.4 nm. (Top) Intrapeptide $C_\beta-C_\beta$ distances in nm. For K28-A42, the N of the side chain and the carboxyl carbon atom were used. These distances were not used for constructing the progress index. (Top) Representative snapshots extracted from the simulations corresponding to (a) little deviation from the initial structure, (b) small detachment of residues ^{21}AEDVG^{25} from their neighbors, and (c) complete detachment of the central 15 residues.

of the peak along the sequence and around residues ^{36}VG^{37} (only at the even end), are probably due to insufficient sampling, as they are less pronounced or absent in the simulations at 370 K (Figure S4).

SAPPHIRE Analysis of Disorder at the Tip. The SAPPHIRE (States and Pathways Projected with High Resolution) plot[53,54] has been developed to capture in a single illustration the states sampled by a complex system and the order in which they are visited along one or multiple trajectories. The essential idea is to generate a one-dimensional plot which allows the partition of the entire sampling into free energy basins based on the similarity between the simulation snapshots as defined by a metric given as input. Briefly, starting from a random snapshot (i.e., simulation frame), the remaining snapshots are ordered by allowing the frame closest to any prior entry in the sequence to become the next item in the array of data. This allows the sorting of the data into sets of basins consisting of similar snapshots without any a priori clustering or overlap between the distinct states. The resulting sequence of snapshots is referred to as the progress index. The progress index is usually annotated with several geometric variables which are helpful to visually characterize the states. Here we define the metric as the RMSD of the $C_\alpha-C_\alpha$ distance across analogue residues from neighboring peptides. The N-terminal segment 1–14 is disordered, while the β_3 strand is almost always conserved (Figure 4). These stretches can be excluded from the metric as they do not contain any discriminatory signal. Thus, residues 15–29 are selected for the metric used to construct the progress index and generate the SAPPHIRE plot. First we analyze the SAPPHIRE plot for peptide A using as a metric the $C_\alpha-C_\alpha$ distances of the corresponding residues in peptides A and B (Figure 5 and Movie M3). The barriers on the cut function (i.e., the local maxima on the profile in black in the bottom part of Figure 5) enable the identification of individual metastable states. The statistical weight of each state can be quantified as the progress-index segment between two consecutive barriers. Importantly, recurrence across the individual simulations shows that most basins are sampled several times (red dots in the bottom part of Figure 5). The first 2.5×10^4 frames are grouped into a single basin, which includes the simulation snapshots close to the solid state NMR structure. The structural annotation shows distances below 0.5 nm, indicating that peptide A is optimally bound to peptide B. A representative snapshot is shown in Figure 5a; the peptide arrangement is very similar to the one in the solid state NMR structure. A pronounced barrier in the cut profile separates this basin from all other states. The snapshots, in which the loop connecting the first two β-strands shows a significant increase in distance from its neighbor, accumulate between 2.5×10^4 and 12×10^4 along the progress index (Figure 5b). The collection of small basins that follows contains states in which

DOI: 10.1021/acs.jpcb.8b05236
J. Phys. Chem. B 2018, 122, 11072–11082

several amino acids detach from their neighbors. In particular, the β_1 strand dissociates in the states with a progress index value larger than 12×10^4 (Figure 5c). An additional annotation is plotted on top of the progress index to monitor seven intramolecular distances that have been proposed to contribute to the stabilization of the monomeric double horseshoe topology. The intramolecular contacts are preserved in the first basin on the left which is the closest to the initial structure. In the metastable states that differ from the first basin, the G33-V36 short-range contact is almost always formed, while the L17-L34 interaction and salt bridge between the K28 side chain and the C-terminal carboxyl group are the least stable. Statistical significance for the sampling at the odd end is supported by the SAPPHIRE plot of peptide J (Figure S8). Both peptides show a higher stability of the ^{15}QKLVFF^{20} fragment over most of the sampling (i.e., along most of the progress index) as compared to β_2. We compare the two ends of the fibril by combining the net effect of the two tip peptides into a single SAPPHIRE plot (Figure S9 for the odd end and Figure S12 for the even end). The SAPPHIRE plots show significant sampling of conformations close to the solid state NMR state, which occupies the first basin. The main difference between the two ends is the slightly more pronounced detachment of the segment A21-G29 at the odd end than the even end. Concerning the intrapeptide interactions, similar patterns are observed at both ends, except for the hydrophobic contact between F19 and I32, which is more stable at the even end (Figure S12) than the odd end (Figure S9).

Flexibility at the N-Terminus and Stability of β_1 and β_3 Strands. The N-terminal residues 1−14 are disordered in all of the peptides (Table 1 and Movie M3). The distributions of the radius of gyration values and asphericity show that, for both protofilaments, the N-terminal stretches can assume a wide variety of conformations from rather compact to very extended (Figure 6). The disorder is observed in all of the runs and at both temperature values (Figure S14). The backbone N atoms of residues 1−10 of the peptides at the tip are in contact with atoms on other peptides only between 10% and 40% of the simulation time (Figure 7). Interestingly, the N-terminal segment can transiently associate in a parallel β-sheet arrangement with the adjacent peptide in the same layer at the surface (Figure 8). While the N-terminal segments at the odd end are slightly less disordered than at the even end, the opposite is observed for the segment A21-G29 (Figure 7). This may be a consequence of the fibrillar twist. Similar profiles and differences between odd and even ends emerge from the simulations at 370 K (Figure S6). The highest contact frequency is observed for residues 15−20 and 30−41, corresponding to β_1 and a segment that includes β_3, respectively. This finding is consistent with the analysis of parallel in-register contacts (Figure 4) and provides further evidence that the β_3 residues of the tip peptides have limited flexibility and remain attached to their neighboring peptide. The C-terminal residues 41−42 of peptides I and R (even end) can detach transiently (Figure 7), which is also observed at high temperatures (Figure S6).

Table 1. Average Secondary Structure Content for the Peptides at the Ends

%	β-rich	helical	coil
N-term	6	1	93
	9	1	90
β_1	54	0	46
	65	0	34
β_2	35	1	64
	40	0	60
β_3	61	0	39
	67	0	33

[a]Values represent averages over peptide segments and the 160000 snapshots at 310 K. For each peptide segment, the two rows show the values averaged over the odd end peptides (A and J) or even end peptides (I and R), respectively. See Table S1 for T = 370 K and Figure S15 for the secondary structure assignment per residue.

The plasticity of the sequence stretch A21-G29 for the peptides at the tip (Figure 7) is consistent with the data from the ^{15}N-DEST NMR experiments, probing the exchange between the monomer and protofibril-bound states of Aβ42.[55,56] The NMR data indicate that the segments 16−23 and 33−40 form direct contacts with the fibrillar surface, while residues 24−32 and the N-terminal segment are predominantly tethered, i.e., not directly in contact with the fibrillar surface. Overall, the structural and fluctuational differences between the two ends are not sufficient to extract definitive conclusions on the unidirectional growth of the fibril.

Intermolecular Contacts at the Fibril Tips. To identify contacts between adjacent peptides at the tip, we plot the A-J interpeptide contact map (odd end) and I-R contact map (even end) where a contact is defined using a 0.8 nm threshold between any pairs of atoms (Figure 9). At both ends, the most frequent contacts are consistent with those observed in the solid state NMR structure and reflect the double horseshoe arrangement of the protofilaments.[11,12] In particular, close to the symmetry axis, there are very strong interactions between the residue pairs ^{34}LM^{35}. Furthermore, there are persistent contacts between the segments ^{12}VHHQKL^{17} and ^{34}LMVG^{37}. At the odd end, there are additional contacts between the N-terminal segment of peptide A and the β_3 strand of peptide J, while at the even end, the N-terminal residues of peptide R interact with residues ^{35}MVG^{37} of peptide I. At an elevated temperature, the distribution of interpeptide contacts at the odd end (Figure S7a) shows a rather symmetric pattern, i.e., invariance with respect to swapping A with J. Thus, it is likely that the different contact frequencies observed at 310 K for the two equivalent peptides at the odd end are due to the limited sampling.

Analysis of the contacts between the tip peptides and the penultimate layers shows that additional in-register contacts are formed transiently by the ^{8}SGYEVHH^{14} residues (Figure 10). These simulation results indicate that the β_1 strand can extend to include residues upstream in the sequence. Furthermore, the N-terminal residues ^{4}FRHD^{7} of the peptides in the penultimate layer can associate with the segment ^{10}YEVHHQKLVF^{19} of the tip peptide.

DISCUSSION

The recently published structure of a disease relevant Aβ fibril is significantly different with respect to the structures analyzed previously by means of molecular simulations. A number of similarities and differences arise from a comparison with previous simulation studies.

First, we report on the limited flexibility of the β_1 (residues 15−20) and β_3 (residues 35−41) segments as compared to that of β_2 (residues 24−32). This is consistent with previous simulation results using other structures[57,58] as starting

DOI: 10.1021/acs.jpcb.8b05236
J. Phys. Chem. B 2018, 122, 11072−11082

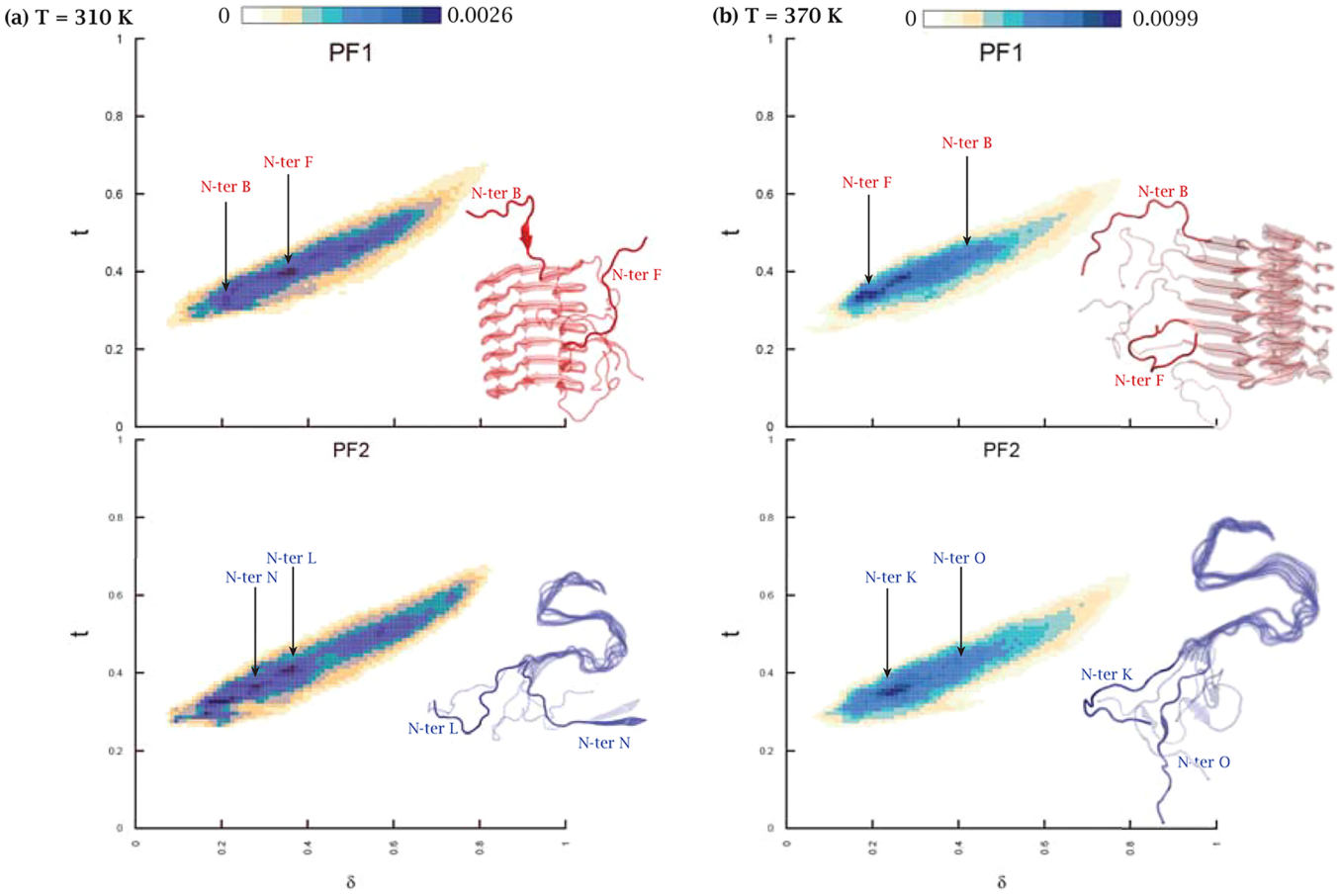

Figure 6. Disorder of the N-terminal segment. Two-dimensional histograms of the normalized radius of gyration, t, vs the asphericity, δ, for the N-terminal stretches 1−14 of peptides B−H for PF1 and peptides K-Q for PF2 at (a) T = 310 K and (b) T = 370 K. Both measures are normalized to an interval of 0 to 1. The snapshots show representative conformations of the selected N-terminal stretches.

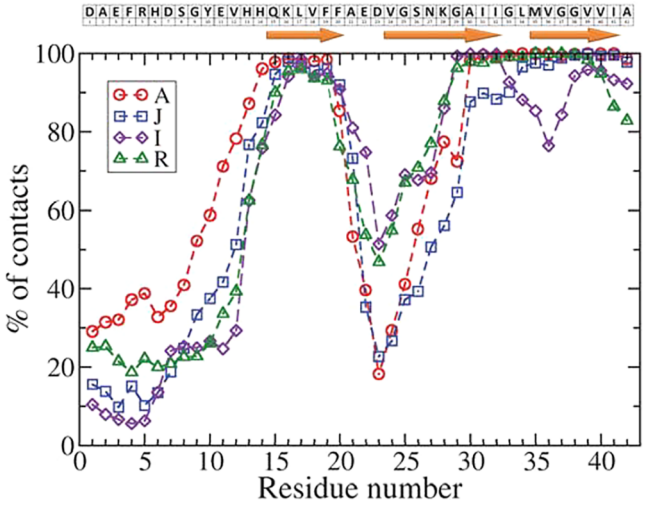

Figure 7. Percentage of interpeptide contacts formed by the tip peptides with the rest of the fibrillar structure. A residue is considered to be in contact with any other residue if the distance between its backbone N atom and any atom of another peptide is below 0.5 nm.

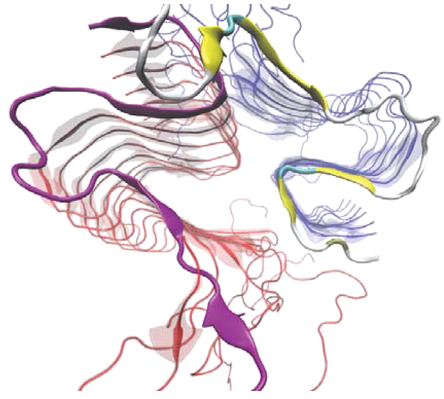

Figure 8. View of the even end of the fibril showing the association of part of the N-terminal segment of peptide R with the core of peptide I in a parallel β-sheet arrangement. The color scheme of peptide R corresponds to the secondary structure assignment of its residues (yellow, cyan, and gray for β-sheet, turn, and loop, respectively).

configurations.[59,60] Bacci et al. observed that the motifs ^{17}LVFF^{20}, ^{31}IIGLMV^{36}, and ^{35}MVGGVV^{40} remain closely associated with the neighboring peptide.[59] Han and Schulten showed in their investigation that the formation of initial fibril contacts is sequence-specific and favorable in the hydrophobic regions;[60] i.e., on average, more contacts are formed between sequences ^{17}LVFFA^{21} and ^{37}GGVVIA^{42} and the neighboring peptides. Baumketner et al. investigated the Aβ40 fibril polymorph[58] and identified the region 21−29 as the first to detach from the fibril, while the segments ^{14}HQKLVFF^{20} and ^{30}AIIGLMV^{36} were suggested to be part of the transition state ensemble of the dissociation process.[31] Buchete et al. investigated the stability and the early dissociation events in

DOI: 10.1021/acs.jpcb.8b05236
J. Phys. Chem. B 2018, 122, 11072−11082

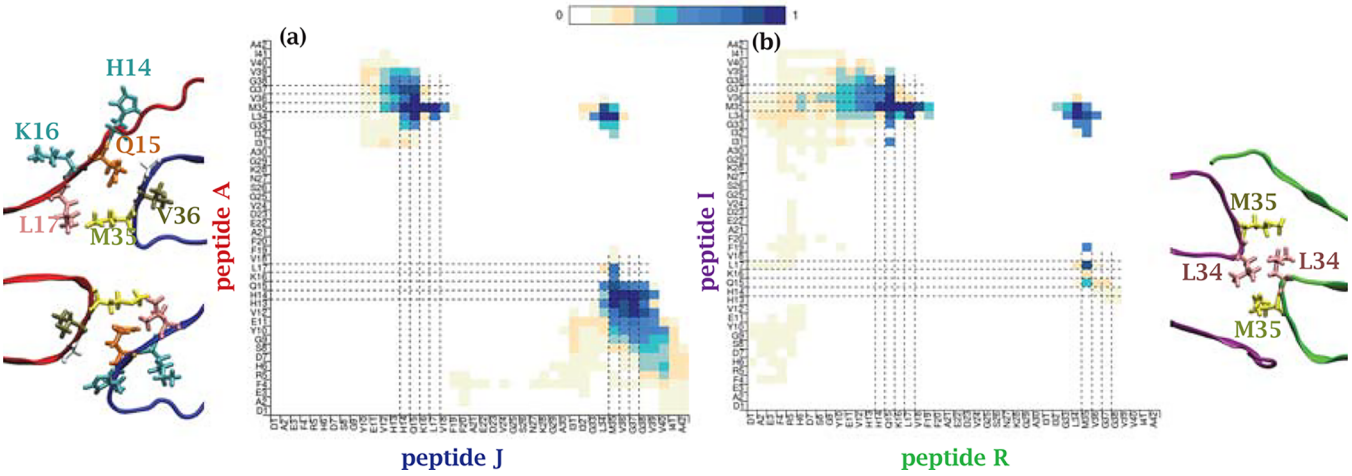

Figure 9. Contact frequencies between adjacent peptides resolved by residues at the (a) odd end and at the (b) even end. Two residues are considered to be in contact if the distance between any of their atoms is below 0.8 nm. High frequencies are highlighted by dark colors. The structures on the left and right highlight the contacts between the two protofilaments as observed in the solid state NMR structure.

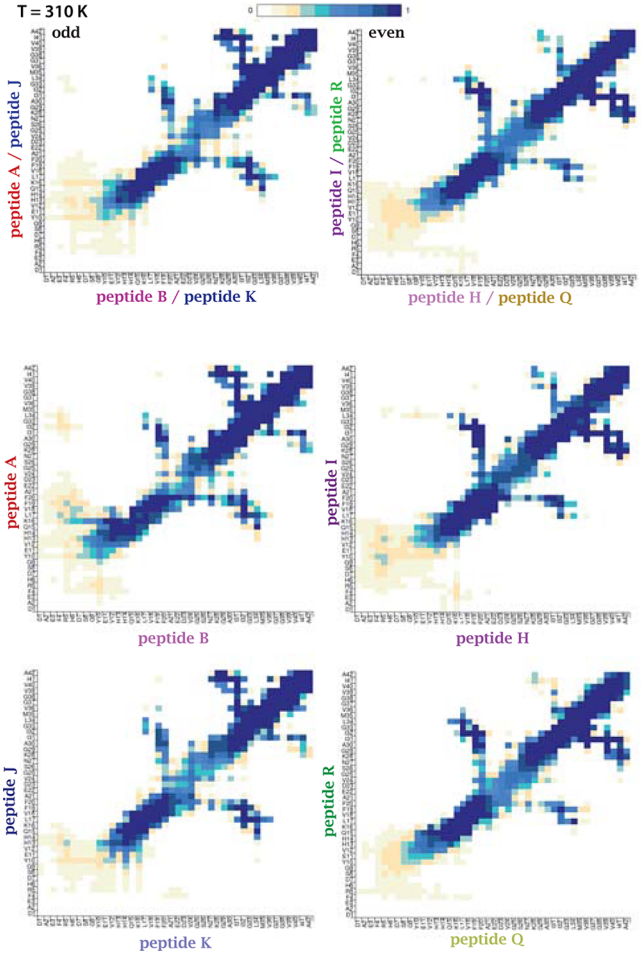

Figure 10. Contact frequencies between peptides at the tip and in the penultimate layer. (Top) Contact maps for the odd end (left) and even end (right) peptides. (Middle and Bottom) Contact maps for single pairs of peptides.

Aβ(9−40) fibrils consisting of two protofilaments.[61] Their simulations showed a loss of structure at the tip layers at high temperatures and structurally stable fibrillar cores at room temperature. The loss of the structure at the tips starts in the 24−30 region and is followed by residues 9−23, while the nine C-terminal residues, i.e., the segment 32−40, remain closely attached to their immediate neighbors. They suggest a possible mechanism for the fibril elongation as a simple time reversal of the dissociation event; i.e., monomer addition to the fibrillar surface is driven by strong hydrophobic interactions stabilizing residues ^{31}IIGLMVGGV^{39}, followed by the association of the less stable 9−23 residues, and finally the flexible segment 24−30. This interpretation, in particular the consolidation of the segment 24−30 as the final part of the association event, is consistent with our simulation results. Experimental findings strengthen the aforementioned claims as there is evidence indicating that the regions ^{17}LVFF^{20} and ^{30}AIIGLM^{35} play a relevant role in the early steps of Aβ misfolding and aggregation[62] and as critical regions for stability and toxicity.[63,64] Taking these discussion points into account, it appears that Aβ42 and Aβ40 share the preference of the detachment of the central residues. This may occur due to the high propensity of this region to form structured conformations in solution.[65]

Second, our results inform on the high flexibility of the N-terminal regions and the transient contacts they form with β_3. The disordered nature of the N-terminal segments is in agreement with the study of Bacci et al.,[59] yet some differences arise in the contacts formed with the hydrophobic core, as the previous study reported on the transient contacts between the N-terminal stretches at the tips and residues ^{17}LVFF^{20}. This discrepancy is due to the different fibrillar structures used in the different studies. Nevertheless, the net effect is the same as the interactions of the N-terminal stretches with the ordered part of the tip peptides would prevent a free peptide from attaching to the surface of the fibril and continue fibrillar growth. Therefore, the N-terminal stretches contribute to the free-energy barrier that a peptide has to overcome in order to transform from its solvated conformation into the fibril-bound state. This statement is consistent, also, with experimental studies which demonstrate that N-terminus truncated peptides enhance aggregation[66] and accelerate fibril formation.[67,68] Extending the discussion to the "stop-and-go" mechanism of amyloid growth,[69−72] we hypothesize that the N-terminal stretches of the peptides at the tip actively contribute to the

DOI: 10.1021/acs.jpcb.8b05236
J. Phys. Chem. B 2018, 122, 11072−11082

"stop" phase by shielding the fibrillar template and hindering growth by monomer addition to the fibrillar end.

CONCLUSIONS

We have analyzed the structure and flexibility of a disease-relevant Aβ42 monomorphic fibril[11,12] by multiple molecular dynamics simulations of an 18-meric fibrillar segment. Previous simulation studies of Aβ42 started from structurally different fibrils (see, for example, refs 59,61,73, and 74 for a review). Four main observations emerge from the analysis of a cumulative sampling of 8 μs at physiological conditions and 7.5 μs at a temperature of 370 K. First, the core of the 18-meric fibril, i.e., the central segment consisting of the 14 peptides that are not located at the tips, is structurally stable with marginal deviations from the starting conformation. Second, the twist along the fibrillar axis is negative and measures about 3 degrees. Third, the highest flexibility is observed at the N-terminal stretch 1−14 which is consistent with the NMR spectroscopy data.[11,12] Despite the predominance of disorder, the detailed analysis of the secondary structure content of the peptides at the tips shows that their N-terminal segment can assume the β-extended conformation (6−9%, Table 1) and sporadically helical structure (<1%). Furthermore, the N-terminal residues of a peptide at the tip can associate with the β_3 strand of the adjacent peptide (Figures 8 and 9). These simulation results go beyond the simple description of the disordered N-terminal tail, which emerges from most experimental works. In particular, the simulations suggest that the interpeptide contacts at the tip might contribute to the arrest phase of the stop-and-go mechanism. Fourth, at both tips, there is disorder in the segment 21−29, which includes most of the β_2 strand (residues 24−32). In contrast, the β_3 strand (residues 35−41) remains closely associated with the fibril (Figure 7). Thus, the displacement of the segment 21−29 is proposed as the initial step of monomer detachment.

ASSOCIATED CONTENT

Supporting Information

The Supporting Information is available free of charge on the ACS Publications website at DOI: 10.1021/acs.jpcb.8b05236.

RMSDs, results at 370 K, SAPPHIRE plots, peptide−peptide contacts, compactness of the N-termini, and secondary structure assignment (PDF)

Behavior of the surface peptides ranging from M10 at the odd end and M1 at the even end to M8 (MPG)

Behavior of the surface peptides ranging from M10 at the odd end and M1 at the even end to M4 (MPG)

SAPPHIRE plot for peptide A using as a metric the C_α−C_α distances of the corresponding residues in peptides A and B (MPG)

AUTHOR INFORMATION

Corresponding Authors

*E-mail: i.ilie@bioc.uzh.ch.

*E-mail: caflisch@bioc.uzh.ch.

ORCID

Ioana M. Ilie: 0000-0002-5935-3332

Amedeo Caflisch: 0000-0002-2317-6792

Notes

The authors declare no competing financial interest.

ACKNOWLEDGMENTS

We thank Dr. Andreas Vitalis for preparing the starting structure and interesting discussions. This work was supported in part by a grant of the Swiss National Science Foundation to A.C. Ioana M. Ilie thanks the Peter und Traudl Engelhorn Foundation for a postdoctoral fellowship. The computational resources were provided by the Swiss National Supercomputing Centre (CSCS) in Lugano.

REFERENCES

(1) Hofrichter, J.; Ross, P. D.; Eaton, W. A. Kinetics and Mechanism of Deoxyhemoglobin S Gelation: A New Approach to Understanding Sickle Cell Disease. *Proc. Natl. Acad. Sci. U. S. A.* **1974**, *71*, 4864−4868.

(2) Eaton, W. A.; Hofrichter, J. Sickle Cell Hemoglobin Polymerization. *Advances in Protein Chemistry*; Academic Press, 1990; Vol. *40*; pp 63−279.

(3) Eaton, W. A.; Bunn, H. F. Treating sickle cell disease by targeting HbS polymerization. *Blood* **2017**, *129*, 2719−2726.

(4) Dobson, C. M. Protein misfolding, evolution and disease. *Trends Biochem. Sci.* **1999**, *24*, 329−332.

(5) Chiti, F.; Dobson, C. M. Protein Misfolding, Functional Amyloid, and Human Disease. *Annu. Rev. Biochem.* **2006**, *75*, 333−366.

(6) Knowles, T. P. J.; Vendruscolo, M.; Dobson, C. M. The amyloid state and its association with protein misfolding diseases. *Nat. Rev. Mol. Cell Biol.* **2014**, *15*, 384−396.

(7) Bloom, G. Amyloid-β and tau: The trigger and bullet in alzheimer disease pathogenesis. *JAMA Neurology* **2014**, *71*, 505−508.

(8) El-Agnaf, O. M.; Mahil, D. S.; Patel, B. P.; Austen, B. M. Oligomerization and Toxicity of β-Amyloid-42 Implicated in Alzheimer's Disease. *Biochem. Biophys. Res. Commun.* **2000**, *273*, 1003−1007.

(9) Kuperstein, I.; Broersen, K.; Benilova, I.; Rozenski, J.; Jonckheere, W.; Debulpaep, M.; Vandersteen, A.; Segers-Nolten, I.; Van Der Werf, K.; Subramaniam, V.; et al. Neurotoxicity of Alzheimer's disease Aβ peptides is induced by small changes in the Aβ42 to Aβ40 ratio. *EMBO J.* **2010**, *29*, 3408−3420.

(10) Selkoe, D. J.; Hardy, J. The amyloid hypothesis of Alzheimer's disease at 25 years. *EMBO Mol. Med.* **2016**, *8*, 595−608.

(11) Wälti, M. A.; Ravotti, F.; Arai, H.; Glabe, C. G.; Wall, J. S.; Böckmann, A.; Güntert, P.; Meier, B. H.; Riek, R. Atomic-resolution structure of a disease-relevant Aβ(1−42) amyloid fibril. *Proc. Natl. Acad. Sci. U. S. A.* **2016**, *113*, E4976−E4984.

(12) Colvin, M. T.; Silvers, R.; Ni, Q. Z.; Can, T. V.; Sergeyev, I.; Rosay, M.; Donovan, K. J.; Michael, B.; Wall, J.; Linse, S.; et al. Atomic Resolution Structure of Monomorphic Aβ42 Amyloid Fibrils. *J. Am. Chem. Soc.* **2016**, *138*, 9663−9674.

(13) Gremer, L.; Schölzel, D.; Schenk, C.; Reinartz, E.; Labahn, J.; Ravelli, R. B. G.; Tusche, M.; Lopez-Iglesias, C.; Hoyer, W.; Heise, H.; et al. Fibril structure of amyloid-β(1−42) by cryo−electron microscopy. *Science* **2017**, *358*, 116−119.

(14) Ilie, I. M.; den Otter, W. K.; Briels, W. J. A coarse grained protein model with internal degrees of freedom. Application to α-synuclein aggregation. *J. Chem. Phys.* **2016**, *144*, 085103.

(15) Saric, A.; Chebaro, Y. C.; Knowles, T. P. J.; Frenkel, D. Crucial role of nonspecific interactions in amyloid nucleation. *Proc. Natl. Acad. Sci. U. S. A.* **2014**, *111*, 17869−17874.

(16) Pellarin, R.; Guarnera, E.; Caflisch, A. Pathways and Intermediates of Fibril Formation. *J. Mol. Biol.* **2007**, *374*, 917−924.

(17) Pellarin, R.; Caflisch, A. Interpreting the Aggregation Kinetics of Amyloid Peptides. *J. Mol. Biol.* **2006**, *360*, 882−892.

(18) Ilie, I. M.; den Otter, W. K.; Briels, W. J. The attachment of α-synuclein to a fiber: A coarse grain approach. *J. Chem. Phys.* **2017**, *146*, 115102.

(19) Zhang, J.; Muthukumar, M. Simulations of nucleation and elongation of amyloid fibrils. *J. Chem. Phys.* **2009**, *130*, 035102.

DOI: 10.1021/acs.jpcb.8b05236
J. Phys. Chem. B 2018, 122, 11072−11082

(20) Auer, S.; Meersman, F.; Dobson, C. M.; Vendruscolo, M. A Generic Mechanism of Emergence of Amyloid Protofilaments from Disordered Oligomeric Aggregates. *PLoS Comput. Biol.* **2008**, *4*, e1000222.
(21) Bellesia, G.; Shea, J.-E. Self-assembly of β-sheet forming peptides into chiral fibrillar aggregates. *J. Chem. Phys.* **2007**, *126*, 245104.
(22) Barz, B.; Urbanc, B. Minimal Model of Self-Assembly: Emergence of Diversity and Complexity. *J. Phys. Chem. B* **2014**, *118*, 3761−3770.
(23) Vitalis, A.; Caflisch, A. Micelle-Like Architecture of the Monomer Ensemble of Alzheimer's Amyloid-β Peptide in Aqueous Solution and Its Implications for Aβ Aggregation. *J. Mol. Biol.* **2010**, *403*, 148−165.
(24) Ilie, I. M.; Nayar, D.; den Otter, W. K.; van der Vegt, N. F.; Briels, W. J. Intrinsic Conformational Preferences and Interactions in α-synuclein Fibrils. Insights from Molecular Dynamics Simulations. *J. Chem. Theory Comput.* **2018**, *14*, 3298−3310.
(25) Sgourakis, N. G.; Merced-Serrano, M.; Boutsidis, C.; Drineas, P.; Du, Z.; Wang, C.; Garcia, A. E. Atomic-Level Characterization of the Ensemble of the Aβ(1−42) Monomer in Water Using Unbiased Molecular Dynamics Simulations and Spectral Algorithms. *J. Mol. Biol.* **2011**, *405*, 570−583.
(26) Vaiana, S. M.; Best, R. B.; Yau, W.-M.; Eaton, W. A.; Hofrichter, J. Evidence for a Partially Structured State of the Amylin Monomer. *Biophys. J.* **2009**, *97*, 2948−2957.
(27) Soto, P.; Griffin, M. A.; Shea, J.-E. New Insights into the Mechanism of Alzheimer Amyloid-β Fibrillogenesis Inhibition by N-Methylated Peptides. *Biophys. J.* **2007**, *93*, 3015−3025.
(28) Shimizu, T.; Fukuda, H.; Murayama, S.; Izumiyama, N.; Shirasawa, T. Isoaspartate formation at position 23 of amyloid beta peptide enhanced fibril formation and deposited onto senile plaques and vascular amyloids in Alzheimer's disease. *J. Neurosci. Res.* **2002**, *70*, 451−461.
(29) Berhanu, W. M.; Alred, E. J.; Hansmann, U. H. E. Stability of Osaka Mutant and Wild-Type Fibril Models. *J. Phys. Chem. B* **2015**, *119*, 13063−13070.
(30) Coskuner-Weber, O.; Uversky, V. N. Insights into the Molecular Mechanisms of Alzheimer's and Parkinson's Diseases with Molecular Simulations: Understanding the Roles of Artificial and Pathological Missense Mutations in Intrinsically Disordered Proteins Related to Pathology. *Int. J. Mol. Sci.* **2018**, *19*, E336.
(31) Baumketner, A.; Krone, M. G.; Shea, J.-E. Role of the familial Dutch mutation E22Q in the folding and aggregation of the 15−28 fragment of the Alzheimer amyloid-β protein. *Proc. Natl. Acad. Sci. U. S. A.* **2008**, *105*, 6027−6032.
(32) Lin, Y.-S.; Pande, V. S. Effects of Familial Mutations on the Monomer Structure of Aβ42. *Biophys. J.* **2012**, *103*, L47−L49.
(33) Caballero-Herrera, A.; Nordstrand, K.; Berndt, K. D.; Nilsson, L. Effect of Urea on Peptide Conformation in Water: Molecular Dynamics and Experimental Characterization. *Biophys. J.* **2005**, *89*, 842−857.
(34) Levine, Z. A.; Larini, L.; LaPointe, N. E.; Feinstein, S. C.; Shea, J.-E. Regulation and aggregation of intrinsically disordered peptides. *Proc. Natl. Acad. Sci. U. S. A.* **2015**, *112*, 2758−2763.
(35) Merchant, K. A.; Best, R. B.; Louis, J. M.; Gopich, I. V.; Eaton, W. A. Characterizing the unfolded states of proteins using single-molecule FRET spectroscopy and molecular simulations. *Proc. Natl. Acad. Sci. U. S. A.* **2007**, *104*, 1528−1533.
(36) Zheng, W.; Borgia, A.; Buholzer, K.; Grishaev, A.; Schuler, B.; Best, R. B. Probing the Action of Chemical Denaturant on an Intrinsically Disordered Protein by Simulation and Experiment. *J. Am. Chem. Soc.* **2016**, *138*, 11702−11713.
(37) Eisenberg, D. S.; Sawaya, M. R. Implications for Alzheimer's disease of an atomic resolution structure of amyloid-β(1−42) fibrils. *Proc. Natl. Acad. Sci. U. S. A.* **2016**, *113*, 9398−9400.
(38) Berendsen, H.; van der Spoel, D.; van Drunen, R. GROMACS: A message-passing parallel molecular dynamics implementation. *Comput. Phys. Commun.* **1995**, *91*, 43−56.
(39) Hess, B.; Kutzner, C.; van der Spoel, D.; Lindahl, E. GROMACS 4: Algorithms for Highly Efficient, Load-Balanced, and Scalable Molecular Simulation. *J. Chem. Theory Comput.* **2008**, *4*, 435−447.
(40) Huang, J.; Rauscher, S.; Nawrocki, G.; Ran, T.; Feig, M.; de Groot, B. L.; Grubmueller, H.; MacKerell, A. D., Jr CHARMM36m: An Improved Force Field for Folded and Intrinsically Disordered Proteins. *Nat. Methods* **2017**, *14*, 71−73.
(41) Vitalis, A.; Pappu, R. V. Chapter 3 Methods for Monte Carlo Simulations of Biomacromolecules. *Annual Reports in Computational Chemistry*; Elsevier, 2009; Vol. 5; pp 49−76.
(42) Vitalis, A.; Pappu, R. V. ABSINTH: A new continuum solvation model for simulations of polypeptides in aqueous solutions. *J. Comput. Chem.* **2009**, *30*, 673−699.
(43) Best, R. B.; Zhu, X.; Shim, J.; Lopes, P. E. M.; Mittal, J.; Feig, M.; MacKerell, A. D. Optimization of the Additive CHARMM All-Atom Protein Force Field Targeting Improved Sampling of the Backbone ϕ, ψ and Side-Chain χ1 and χ2 Dihedral Angles. *J. Chem. Theory Comput.* **2012**, *8*, 3257−3273.
(44) Jorgensen, W. L.; Chandrasekhar, J.; Madura, J. D.; Impey, R. W.; Klein, M. L. Comparison of simple potential functions for simulating liquid water. *J. Chem. Phys.* **1983**, *79*, 926−935.
(45) Bussi, G.; Donadio, D.; Parrinello, M. Canonical sampling through velocity rescaling. *J. Chem. Phys.* **2007**, *126*, 014101.
(46) Berendsen, H. J. C.; Postma, J. P. M.; van Gunsteren, W. F.; DiNola, A.; Haak, J. R. Molecular dynamics with coupling to an external bath. *J. Chem. Phys.* **1984**, *81*, 3684−3690.
(47) Hess, B.; Bekker, H.; Berendsen, H. J. C.; Fraaije, J. G. E. M. LINCS: A linear constraint solver for molecular simulations. *J. Comput. Chem.* **1997**, *18*, 1463−1472.
(48) Caflisch, A.; Karplus, M. Molecular dynamics simulation of protein denaturation: solvation of the hydrophobic cores and secondary structure of barnase. *Proc. Natl. Acad. Sci. U. S. A.* **1994**, *91*, 1746−1750.
(49) Caflisch, A.; Karplus, M. Acid and Thermal Denaturation of Barnase Investigated by Molecular Dynamics Simulations. *J. Mol. Biol.* **1995**, *252*, 672−708.
(50) Periole, X.; Huber, T.; Bonito-Oliva, A.; Aberg, K. C.; van der Wel, P. C. A.; Sakmar, T. P.; Marrink, S. J. Energetics Underlying Twist Polymorphisms in Amyloid Fibrils. *J. Phys. Chem. B* **2018**, *122*, 1081−1091.
(51) Zhang, R.; Hu, X.; Khant, H.; Ludtke, S. J.; Chiu, W.; Schmid, M. F.; Frieden, C.; Lee, J.-M. Interprotofilament interactions between Alzheimer's Aβ1−42 peptides in amyloid fibrils revealed by cryoEM. *Proc. Natl. Acad. Sci. U. S. A.* **2009**, *106*, 4653−4658.
(52) Schmidt, M.; Sachse, C.; Richter, W.; Xu, C.; Fändrich, M.; Grigorieff, N. Comparison of Alzheimer Aβ(1−40) and Aβ(1−42) amyloid fibrils reveals similar protofilament structures. *Proc. Natl. Acad. Sci. U. S. A.* **2009**, *106*, 19813−19818.
(53) Bloechliger, N.; Vitalis, A.; Caflisch, A. A scalable algorithm to order and annotate continuous observations reveals the metastable states visited by dynamical systems. *Comput. Phys. Commun.* **2013**, *184*, 2446−2453.
(54) Bloechliger, N.; Vitalis, A.; Caflisch, A. High-Resolution Visualisation of the States and Pathways Sampled in Molecular Dynamics Simulations. *Sci. Rep.* **2015**, *4*, 1−5.
(55) Fawzi, N. L.; Ying, J.; Ghirlando, R.; Torchia, D. A.; Clore, G. M. Atomic-resolution dynamics on the surface of amyloid-β protofibrils probed by solution NMR. *Nature* **2011**, *480*, 268.
(56) Fawzi, N. L.; Ying, J.; Torchia, D. A.; Clore, G. M. Probing exchange kinetics and atomic resolution dynamics in high-molecular-weight complexes using dark-state exchange saturation transfer NMR spectroscopy. *Nat. Protoc.* **2012**, *7*, 1523.
(57) Lührs, T.; Ritter, C.; Adrian, M.; Riek-Loher, D.; Bohrmann, B.; Döbeli, H.; Schubert, D.; Riek, R. 3D structure of Alzheimer's amyloid-β(1−42) fibrils. *Proc. Natl. Acad. Sci. U. S. A.* **2005**, *102*, 17342−17347.
(58) Petkova, A. T.; Ishii, Y.; Balbach, J. J.; Antzutkin, O. N.; Leapman, R. D.; Delaglio, F.; Tycko, R. A structural model for

DOI: 10.1021/acs.jpcb.8b05236
J. Phys. Chem. B 2018, 122, 11072−11082

Alzheimer's β-amyloid fibrils based on experimental constraints from solid state NMR. *Proc. Natl. Acad. Sci. U. S. A.* **2002**, *99*, 16742−16747.
(59) Bacci, M.; Vymetal, J.; Mihajlovic, M.; Caflisch, A.; Vitalis, A. Amyloid β Fibril Elongation by Monomers Involves Disorder at the Tip. *J. Chem. Theory Comput.* **2017**, *13*, 5117−5130.
(60) Han, W.; Schulten, K. Fibril Elongation by Aβ17−42: Kinetic Network Analysis of Hybrid-Resolution Molecular Dynamics Simulations. *J. Am. Chem. Soc.* **2014**, *136*, 12450−12460.
(61) Buchete, N.-V.; Hummer, G. Structure and Dynamics of Parallel β-Sheets, Hydrophobic Core, and Loops in Alzheimer's Aβ Fibrils. *Biophys. J.* **2007**, *92*, 3032−3039.
(62) Soto, C. Unfolding the role of protein misfolding in neurodegenerative. *Nat. Rev. Neurosci.* **2003**, *4*, 49−60.
(63) Ma, B.; Nussinov, R. Stabilities and conformations of Alzheimer's β-amyloid peptide oligomers (Aβ16−22, Aβ16−35, and Aβ10−35): Sequence effects. *Proc. Natl. Acad. Sci. U. S. A.* **2002**, *99*, 14126−14131.
(64) Liu, R.; McAllister, C.; Lyubchenko, Y.; Sierks, M. R. Residues 17−20 and 30−35 of beta-amyloid play critical roles in aggregation. *J. Neurosci. Res.* **2004**, *75*, 162−171.
(65) Baumketner, A.; Bernstein, S. L.; Wyttenbach, T.; Lazo, N. D.; Teplow, D. B.; Bowers, M. T.; Shea, J.-E. Structure of the 21−30 fragment of amyloid β-protein. *Protein Sci.* **2006**, *15*, 1239−1247.
(66) Pike, C. J.; Overman, M. J.; Cotman, C. W. Amino-terminal Deletions Enhance Aggregation of β-Amyloid Peptides in Vitro. *J. Biol. Chem.* **1995**, *270*, 23895−23898.
(67) Barritt, J. D.; Viles, J. H. Truncated Amyloid-β(11−40/42) from Alzheimer Disease Binds Cu2+ with a Femtomolar Affinity and Influences Fiber Assembly. *J. Biol. Chem.* **2015**, *290*, 27791−27802.
(68) Barritt, J. D.; Younan, N. D.; Viles, J. H. N-Terminally Truncated Amyloid-β(11−40/42) Cofibrillizes with its Full-Length Counterpart: Implications for Alzheimer's Disease. *Angew. Chem., Int. Ed.* **2017**, *56*, 9816−9819.
(69) Ferkinghoff-Borg, J.; Fonslet, J.; Andersen, C. B.; Krishna, S.; Pigolotti, S.; Yagi, H.; Goto, Y.; Otzen, D.; Jensen, M. H. Stop-and-go kinetics in amyloid fibrillation. *Phys. Rev. E* **2010**, *82*, 010901.
(70) Woerdehoff, M. M.; Bannach, O.; Shaykhalishahi, H.; Kulawik, A.; Schiefer, S.; Willbold, D.; Hoyer, W.; Birkmann, E. Single Fibril Growth Kinetics of α-Synuclein. *J. Mol. Biol.* **2015**, *427*, 1428−1435.
(71) Ban, T.; Hoshino, M.; Takahashi, S.; Hamada, D.; Hasegawa, K.; Naiki, H.; Goto, Y. Direct Observation of Aβ Amyloid Fibril Growth and Inhibition. *J. Mol. Biol.* **2004**, *344*, 757−767.
(72) Pinotsi, D.; Buell, A. K.; Galvagnion, C.; Dobson, C. M.; Kaminski Schierle, G. S.; Kaminski, C. F. Direct Observation of Heterogeneous Amyloid Fibril Growth Kinetics via Two-Color Super-Resolution Microscopy. *Nano Lett.* **2014**, *14*, 339−345.
(73) Buchete, N.-V.; Tycko, R.; Hummer, G. Molecular Dynamics Simulations of Alzheimer's β-Amyloid Protofilaments. *J. Mol. Biol.* **2005**, *353*, 804−821.
(74) Nasica-Labouze, J.; Nguyen, P. H.; Sterpone, F.; Berthoumieu, O.; Buchete, N.-V.; Cote, S.; De Simone, A.; Doig, A. J.; Faller, P.; Garcia, A.; et al. Amyloid β Protein and Alzheimer's Disease: When Computer Simulations Complement Experimental Studies. *Chem. Rev.* **2015**, *115*, 3518−3563.

DOI: 10.1021/acs.jpcb.8b05236
J. Phys. Chem. B 2018, 122, 11072−11082